



# High Performance Tubular Solid Oxide Fuel Cell Based on $\text{Ba}_{0.5}\text{Sr}_{0.5}\text{Ce}_{0.6}\text{Zr}_{0.2}\text{Gd}_{0.1}\text{Y}_{0.1}\text{O}_{3-\delta}$ Proton Conducting Electrolyte

Taghi Amiri,<sup>1,\*</sup> Kalpana Singh,<sup>2</sup> Navjot Kaur Sandhu,<sup>1</sup> Amir Reza Hanifi,<sup>1</sup> Thomas H. Etsell,<sup>1</sup> Jing-Li Luo,<sup>1</sup> Venkataraman Thangadurai,<sup>2,\*</sup> and Partha Sarkar<sup>3,\*</sup>

<sup>1</sup>Department of Chemical and Materials Engineering, University of Alberta, Edmonton, Alberta T6G 1H9, Canada

<sup>2</sup>Department of Chemistry, University of Calgary, 2500 University Drive, NW Calgary, Alberta T2N 1N4, Canada

<sup>3</sup>InnoTech Alberta, Edmonton, Alberta T6N 1E4, Canada

In this work, synthesis and characterization of an anode supported tubular solid oxide fuel cell based on  $\text{Ba}_{0.5}\text{Sr}_{0.5}\text{Ce}_{0.6}\text{Zr}_{0.2}\text{Gd}_{0.1}\text{Y}_{0.1}\text{O}_{3-\delta}$  (BSCZGY) electrolyte has been investigated. Anode-supported Ni - yttria-stabilized zirconia (YSZ) anode was fabricated via slip casting; BSCZGY electrolyte and BSCZGY -  $\text{La}_{0.6}\text{Sr}_{0.4}\text{Co}_{0.2}\text{Fe}_{0.8}\text{O}_3$  (LSCF) composite cathode were coated on support using dip coating, respectively. The chemical compatibility of fuel cell components at sintering temperatures has been investigated by powder X-ray diffraction, and no severe reactions were detected. Electrochemical examination under air/ $\text{H}_2 + 3$  vol. %  $\text{H}_2\text{O}$  showed superior performance achieving a maximum power density of  $1 \text{ W/cm}^2$  at  $850^\circ\text{C}$ , among the best compared to tubular - geometry oxygen conductor solid oxide fuel cells reported earlier and one of the highest reported for a proton conductor electrolyte in literature. Electrochemical impedance spectroscopy was used to examine the electrochemical performance of the full cell at different temperatures, and a detailed analysis was done to distinguish the contribution of ohmic and polarization resistances of the cell. ASR values were  $3.47 \text{ } \Omega\cdot\text{cm}^2$ ,  $1.81 \text{ } \Omega\cdot\text{cm}^2$ ,  $1.23 \text{ } \Omega\cdot\text{cm}^2$ , and  $1.05 \text{ } \Omega\cdot\text{cm}^2$  at 600, 700, 800, and  $850^\circ\text{C}$ , respectively. Analysis of activation energy associated with charge and mass transfer based on fitting of impedances revealed that concentration polarization is the major contributor to the total resistance. The long-term stability for more than 96 hours of operation under load showed no significant degradation, which demonstrated the steady behavior of the cell.

© The Author(s) 2018. Published by ECS. This is an open access article distributed under the terms of the Creative Commons Attribution 4.0 License (CC BY, <http://creativecommons.org/licenses/by/4.0/>), which permits unrestricted reuse of the work in any medium, provided the original work is properly cited. [DOI: 10.1149/2.0331810jes]



Manuscript submitted April 9, 2018; revised manuscript received June 27, 2018. Published July 7, 2018.

A solid oxide fuel cell (SOFC) is a solid-state electrochemical device which converts the chemical energy stored in the fuel directly into electrical energy resulting in high efficiency which along with low environmental impact, quiet operation, and low maintenance makes SOFC highly suitable for stationary power generation applications.<sup>1</sup> Traditional SOFCs employ Ni-YSZ cermet, oxide-ion conducting yttria-stabilized zirconia (YSZ), and lanthanum strontium manganite as the anode, electrolyte and cathode, respectively.<sup>2</sup> To reduce the overpotentials associated with these materials, the cell needs to run at elevated temperatures near  $1000^\circ\text{C}$ .<sup>3</sup> This negatively affects the choice of available materials mostly for interconnects and sealants and their long-term stability.<sup>4</sup> To reduce the operating temperature of SOFC, one of the alternative is to develop new materials for cell components. Oxide ion conducting electrolytes  $\text{La}_{0.9}\text{Sr}_{0.1}\text{Ga}_{0.8}\text{Mg}_{0.2}\text{O}_{3-\delta}$ ,  $\text{Ce}_{0.8}\text{Gd}_{0.2}\text{O}_{2-\delta}$ , and  $\text{Ce}_{0.8}\text{Sm}_{0.2}\text{O}_{1.9}$ , and mixed ionic and electronic conductor cathodes  $\text{Ba}_{0.5}\text{Sr}_{0.5}\text{Co}_{0.8}\text{Fe}_{0.2}\text{O}_{3-\delta}$ ,  $\text{La}_{0.99}\text{Ca}_{0.01}\text{NbO}_4$  and nickelates are some examples. These materials have their own drawbacks mostly related to chemical compatibility and cost resulting in limited large-scale usage.<sup>5</sup> Unlike YSZ which conducts oxygen ions, there has recently been a new trend in developing electrolytes that conduct protons as shown by following equation with Kröger Vink notation:<sup>6</sup>



where  $\text{V}_{\text{O}}^{\bullet\bullet}$  indicates vacancy of oxide ion with effective two positive charges, and  $\text{OH}_{\text{O}}^{\bullet}$  indicates proton attached to the regular oxygen ion site with positive relative charge.

Proton conducting electrolytes (PCEs) have two main advantages, first, they do not dilute the fuel which lowers the performance based on the Nernst equation.<sup>7</sup> Also, due to their relatively low activation energy of conduction due to smaller size of  $\text{H}^+$ , they can achieve high conductivity at lower temperatures.<sup>8-10</sup> Iwahara et al. first reported high proton conductivity ( $\sigma \sim 10^{-2} \text{ S cm}^{-1}$  at  $600^\circ\text{C}$ ) in perovskite type-doped-SrCeO<sub>3</sub> and BaCeO<sub>3</sub> ceramics under humid atmospheres in the early and late 1980s.<sup>11,12</sup> But cerate based perovskites face the problem of poor chemical stability in the presence of moisture and

$\text{CO}_2$ , which is a major hindrance for commercial realization.<sup>13,14</sup> As humidity is present in every fuel cell, and  $\text{CO}_2$  is produced when hydrocarbons are used as fuel, this is an important issue for researchers to solve. On the other hand, Zirconate based perovskites are stable, both mechanically and chemically.<sup>15</sup> However, Zirconate based perovskites such as  $\text{BaZrO}_3$  show lower electrical conductivity than cerate based oxides, due to large grain boundary resistance, which arises due to low sinterability and hence is also rather hard to sinter a leak-free PCE usually needing temperatures exceeding  $1600^\circ\text{C}$ , hampering its actual usage.<sup>16-18</sup> Thus researchers have worked toward the solid solutions between  $\text{BaCeO}_3$  and  $\text{BaZrO}_3$  in order to achieve good chemical stability and high proton conductivity.<sup>17,19</sup>

Tubular SOFC has two main advantages over planar design. First, ease of sealing especially if the tube has only one open ending which greatly reduce the chance of cell failure due to the sealant degradation and enable to run the cell under high pressure operation.<sup>20</sup> Second, it has more resistance toward thermal shocks which improve the start-up times.<sup>21</sup> The main drawback of this design would be its lower performance compare to its counterpart mainly due to the longer path current must take to the current collector.<sup>22</sup>

Power density of the tubular SOFC is inversely related to the diameter.<sup>23</sup> Zhang et al.<sup>24</sup> reported high peak power density of  $513 \text{ mW/cm}^2$  at  $850^\circ\text{C}$  for a tube with outer diameter of 1.3 mm and 1.03 V for the open circuit voltage (OCV) with a YSZ electrolyte. Duan et al.<sup>25</sup> achieved  $522 \text{ mW/cm}^2$  at  $850^\circ\text{C}$ . With the help of PdO impregnation, this result jumped to  $1220 \text{ mW/cm}^2$  at the same temperature. The outer cell diameter was 10.5 mm and the electrolyte was YSZ. Hanifi et al.<sup>14</sup> reported maximum performance of  $416 \text{ mW/cm}^2$  at  $700^\circ\text{C}$  using  $\text{BaZr}_{0.1}\text{Ce}_{0.7}\text{Y}_{0.1}\text{Yb}_{0.1}\text{O}_{3-\delta}$  but saw rapid degradation under  $\text{CO-H}_2$  mixtures.

In the previous work, we have developed and reported a PCE based on  $\text{Ba}_{0.5}\text{Sr}_{0.5}\text{Ce}_{0.6}\text{Zr}_{0.2}\text{Gd}_{0.1}\text{Y}_{0.1}\text{O}_{3-\delta}$  (BSCZGY) with excellent chemical stability under humidity and carbon dioxide.<sup>26</sup> For improving chemical stability, Sr at the A-site and Zr at the B-site were doped in  $\text{BaCeO}_3$ .<sup>26</sup> And for increasing ionic conductivity, aliovalent Gd and Y were doped at B-site of  $\text{BaCeO}_3$ .<sup>26</sup> In the subsequent report, mechanically mixed Ni-BSCZGY (50:50 vol. %) anode composite exhibited area specific resistance (ASR) of  $0.8 \text{ } \Omega\cdot\text{cm}^2$  at  $710^\circ\text{C}$  under  $\text{H}_2 + 3$  vol. %  $\text{H}_2\text{O}$ .<sup>27</sup> By the same analogy to oxygen conductor SOFCs, if we use a PCE/Ni cermet as support, we face some

\*Electrochemical Society Member.

<sup>2</sup>E-mail: mamiri1@ualberta.ca

challenges as well. Cerates have large thermal expansion coefficients due to the reduction of  $\text{Ce}^{4+}$  to  $\text{Ce}^{3+}$  which results in cell degradation in long-term operation.<sup>28</sup> Zirconates have poor sinterability and thus do not have ideal mechanical properties as the support.<sup>26</sup> Ni/YSZ can still be used as support instead to provide sufficient rigidity and electron conductivity of the cell without performance penalty but extra caution need to be taken to match the shrinkage of the support and the electrolyte.<sup>29</sup> Bae et al.<sup>30</sup> successfully used Ni/YSZ both for support and anode functioning layer to make a thin film proton conductor fuel cell with heterogeneous structure to mitigate sintering shrinkage mismatch, achieving more than 1 V in open circuit. This study is aimed at using stable proton conductor BSCZGY as the electrolyte in a complete cell consisting of both an anode and cathode to evaluate its electrochemical performance.

### Experimental

**PCE synthesis.**—Proton conducting electrolyte with following nominal chemical composition  $\text{Ba}_{0.5}\text{Sr}_{0.5}\text{Ce}_{0.6}\text{Zr}_{0.2}\text{Gd}_{0.1}\text{Y}_{0.1}\text{O}_{3-\delta}$  (BSCZGY) was synthesized via conventional solid-state synthesis method, as reported in the previous report.<sup>26</sup> Stoichiometric ratios of  $\text{BaCO}_3$ ,  $\text{SrCO}_3$ ,  $\text{CeO}_2$ ,  $\text{ZrO}_2$ ,  $\text{Gd}_2\text{O}_3$ , and  $\text{Y}_2\text{O}_3$  ( $\sim 99.9\%$ , Alfa Aesar) were first mixed and ball-milled with 10 mm zirconia balls and iso-propanol as solvent in 50 ml zirconia ball mill jars (Fritsch planetary ball mill, Pulverisette 5) for 6 h. Iso-propanol from milled powders was evaporated at  $90^\circ\text{C}$  and then powders were pre-treated at  $1050^\circ\text{C}$  for 24 h under air in an alumina crucible, followed by second milling for 6 h. After second milling, powders were uni-axially pressed at 200 kN pressure into cylindrical discs ( $\sim 2$  cm thickness,  $\sim 1$  cm diameter). Cylindrical discs were then calcined twice at  $1450^\circ\text{C}$  for 24 h under air in an alumina crucible, with milling and pelletization step in between. In order to avoid reaction with alumina crucible and Ba evaporation, cylindrical discs were kept on and covered by parent powders. Resulting pellets after final sintering were ground to fine powders in mortar and pestle for powder-X ray diffraction (PXRD), chemical compatibility and electrochemical analyses.

**Support fabrication.**—As-received YSZ (Tosoh TZ-8Y) and NiO (Aldrich,  $< 50$  nm particle size) was mechanically ball-milled together with 35:65 weight ratio in water medium (1:1 ratio) for 24 h. To create enough porosity, 30 volume % graphite (Sigma Aldrich  $< 325$  mesh) was added to the mixture followed by final pH adjustment to 4. Slip casting in plaster mold was used to make the support. By controlling the time, a suitable thickness of support can be cast, and the excess slurry removed. The supports were pre-sintered at  $1000^\circ\text{C}$  for 3 h to gain sufficient strength and remove pore-former and water.

**Anode functional layer (AFL) fabrication.**—NiO, PCE, ethanol and binder (6 wt% ethyl cellulose in terpineol) with appropriate ratio were mixed together and ultrasonicated to remove any undesirable agglomeration or air bubbles. The AFL was dip coated and pre-sintered at  $1000^\circ\text{C}$  for 3 h.

**Electrolyte coating.**—Electrolyte suspension was a mixture of PCE, ethanol and binder. Similar to AFL coating, the coating continued until desirable electrolyte thickness of 10 micron was reached. Sintering was done at  $1450^\circ\text{C}$  for a leakage-free electrolyte.

**Cathode coating.**—A mixture of  $\text{La}_{0.6}\text{Sr}_{0.4}\text{Co}_{0.2}\text{Fe}_{0.8}\text{O}_3$  (LSCF, Fuel Cell Materials)-BZCZGY, azeotrope solvent, polyvinyl butyral as binder, Menhaden fish oil as the dispersant and 30 vol.% graphite was used for cathode ink. The resulting mixture was dip coated on top of electrolyte followed by sintering at  $1000^\circ\text{C}$  to form LSCF-BZCZGY composite cathode. The top and base diameter of the cell was 5.5 mm and 5.23 mm, respectively, with a length of 33 mm and total area of  $1.79\text{ cm}^2$  for the cathode.

**Chemical compatibility between PCE and electrodes.**—The chemical compatibility of the PCE electrolyte with the LSCF (synthesized through sol-gel route) and NiO (Alfa Aesar) powders, was investigated by co-firing the powders at  $1000^\circ\text{C}$  and  $1450^\circ\text{C}$ , respectively, and analyzing the fired powders through PXRD. LSCF and BSCZGY powders (50:50 and 70:30 wt%) were mixed and milled for 6 h with iso-propanol, and were fired at  $1000^\circ\text{C}$  for 3 h with the heating rate of  $5^\circ/\text{minute}$  and cooling rate of  $10^\circ/\text{minute}$ . Similarly, NiO and BSCZGY powders (50:50 wt%) were ball milled for 6 h with iso-propanol followed by co-firing at  $1450^\circ\text{C}$  for 3 h with the heating rate of  $5^\circ/\text{minute}$  and cooling rate of  $10^\circ/\text{minute}$ . Bruker D8 powder X-ray diffractometer with  $\text{CuK}\alpha$  was used to analyze the phase purity of co-fired electrolyte and electrode powders.

**Electrochemical characterization.**—An Agilent electronic load (model # N3301A) was used to measure the OCV and I-V curves. An Agilent scanner (model # E4970A) monitored the thermocouples, while LabView software was used for automated measurements and data collection. Electrochemical impedance spectroscopy (EIS) measurements were used to measure the area specific resistance (ASR) of the cell with a four-probe configuration using a Solartron 1255 frequency response analyzer in combination with a Solartron 1287 electrochemical interface. The frequency range of measurement was between 0.01 Hz - 1 MHz with 12 points per decade. The data were recorded with  $50^\circ\text{C}$  interval in a temperature range of  $600^\circ\text{C} - 850^\circ\text{C}$  using a four-probe setup with  $\text{H}_2+3\text{ vol.}\% \text{H}_2\text{O}$  as fuel and air as the oxidant

**Microstructure characterization.**—The study on the microstructure of the prepared cell was conducted on the fractured samples using a Zeiss Sigma 300 field-emission scanning electrode microscope (SEM). Carbon coating of the samples was done using a Leica EM SCD005 evaporative carbon coater.

### Results and Discussion

**Chemical compatibility.**—Figures 1a and 2b shows the PXRD patterns of mechanically mixed NiO and BSCZGY powders (50:50 wt%) at room temperature, and the co-fired powders at  $1450^\circ\text{C}$ . Figure 1a only shows the diffraction peaks of NiO and BSCZGY phases, and no additional diffraction peak of second-phase impurities such as  $\text{BaNiO}_x$ ,  $\text{BaY}_2\text{NiO}_5$ . As in the previous report,<sup>31</sup> it has been shown that there is a possibility that Ni might substitute Zr site during mechanical mixing or firing at high temperatures owing to their similar ionic radii ( $r_{\text{Zr}^{4+}} = 0.72\text{ \AA}$ ,  $r_{\text{Ni}^{2+}} = 0.69\text{ \AA}$ ). Figure 1b shows the magnified PXRD pattern where it can be seen that there is very slight shift of BSCZGY (110) peak to high  $2\theta$  after firing, which indicates slight or no substitution of Ni in the Zr/Ce site of BSCZGY, indicating no change in stoichiometry of BSCZGY electrolyte.

Similarly, Figure 2 shows the room temperature PXRD patterns of mechanically mixed LSCF and BSCZGY (50:50 and 70:30 wt%) powders, and the co-fired mixtures at  $1000^\circ\text{C}$ . Even though the main cubic ( $Pm\bar{3}m$ ) perovskite phases for both BSCZGY and LSCF remained the same as the mechanically mixed powders at room temperature, the (111) peak of  $\text{CeO}_2$  appeared after firing at  $1000^\circ\text{C}$ . When compare this result to NiO and BSCZGY compatibility result, tendency of LSCF to react with electrolyte at firing temperature above  $800^\circ\text{C}$  might be responsible for some secondary reactions that occur at the interface between cathode and BSCZGY, resulting in appearance of  $\text{CeO}_2$  as a impurity phase.<sup>32,33</sup>

**Electrochemical performance.**—Figure 3 shows the I-V and power density output curves of the cell measured under  $\text{air}/\text{H}_2+3\text{ vol.}\% \text{H}_2\text{O}$ . The optimum temperature for operating the cell was found to be above  $800^\circ\text{C}$  with the maximum performance of  $1\text{ W}/\text{cm}^2$  achieved at  $850^\circ\text{C}$ , making this cell a high temperature SOFC. The almost linear behavior of I-V data especially at higher temperature indicated ohmic behavior, the majority of the loss coming from the electrolyte and the connections. At higher currents, especially

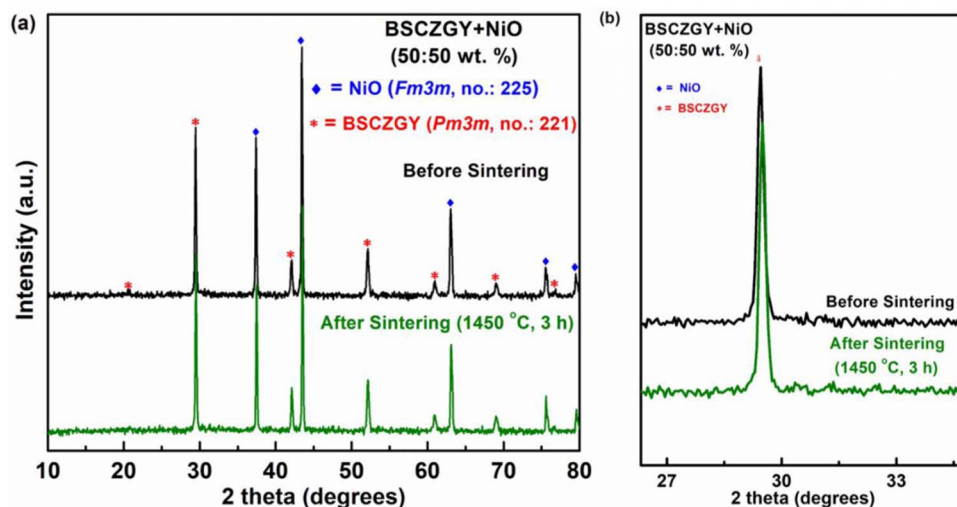


**Figure 1.** (a) XRD patterns of the fresh mixed and fired mixed powders containing NiO, and BSCZGY with a weight % ratio of 50:50. (b) Magnified XRD patterns for (a) showing very slight shift of BSCZGY (110) peak to high  $2\theta$  after firing, indicating slight or no subs.

for 800°C and 850°C, the end of the curves which belongs to fuel starvation, becomes more significant. By increasing the temperature, OCV decreases and the values get closer to theoretical expectation based on the Nernst equation, suggesting a dense electrolyte that prevents charge transfer or gas diffusion directly between the two electrodes.

Nyquist plots of the cell are shown in Figure 4a under open-circuit conditions. The R0-(CPE1-R1)-(CPE2-R2)-(CPE3-R3) equivalent circuit was used to fit the impedance spectrum similar to previous work.<sup>26</sup> As expected, increase in temperature reduces both ohmic and polarization contribution to overall cell resistance. Figure 4b shows that at both 800°C and 850°C, similar ohmic contributions is observed, indicating that electrolyte conductivity appears to have increased slightly after 800°C. This can be ascribed to progressive dehydration at elevated temperatures and increase in oxide ion or electronic conductivity, leading to decrease in proton conductivity due to lower proton concentration.<sup>17,34</sup>

The far-right polarization arc belongs to a mass transfer occurring at the electrodes<sup>35</sup> with  $\omega_{\max} = 6 - 8\text{ Hz}$  and capacitance in the

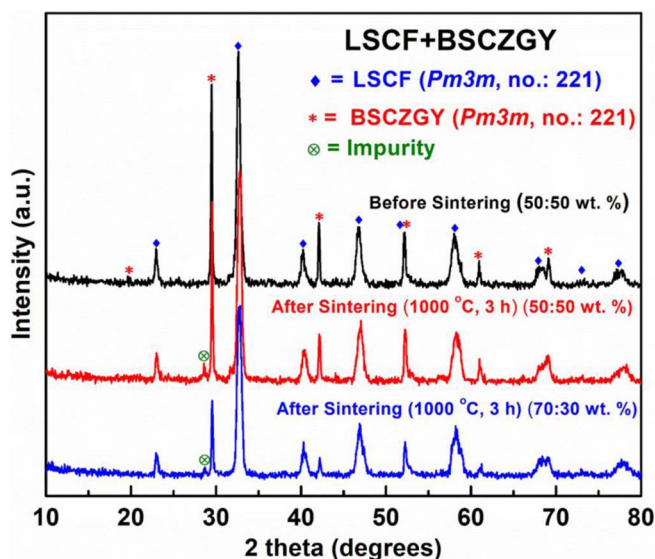
range of 0.1 F; it has arisen both from the cathode contribution<sup>36</sup> and surface electrochemical reactions at the anode.<sup>27</sup> Our results also show that this portion is extremely dependent on the flow of oxidant as shown in Figure 4c. Fuel flow has similar outcomes, but its effect was hampered due to the non-preheating fuel injection and deteriorating effect of cooling of the cell which both lowers the performance and becomes problematic in the long run.

#### Ohmic and polarization contribution and activation energy.—

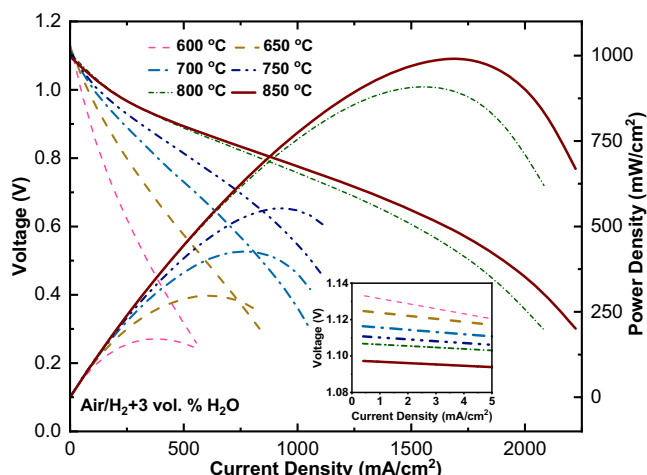
Since proton conduction is a thermally activated process, the proton can be pictured as a trapped charge in an elastic crystal field and thus satisfies the definition of a polaron and resembles a polaron-type conductivity with Arrhenius behavior.<sup>37</sup> LSCF follows a polaron conduction regime as well.<sup>38</sup> Activation energy  $E_a$  depends on the concentration of charge carriers and can be related to electrical conductivity as shown in following equation:<sup>39</sup>

$$\sigma T = \sigma_0 \exp\left(\frac{-E_a}{k_B T}\right) \quad [2]$$

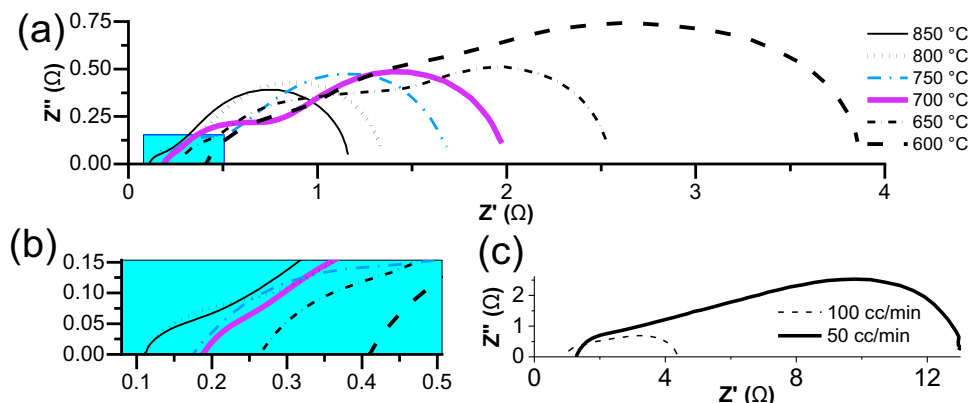
In Equation 2,  $k_B$  is the Boltzmann constant,  $T$  is absolute temperature and  $\sigma_0$  is the pre-exponential factor mostly involving the carrier concentration in the material.<sup>40</sup> Using the data obtained from the



**Figure 2.** XRD patterns of the fresh mixed and fired mixed powders containing LSCF, and BSCZGY with a weight % ratio of 50:50 and 70:30. Where fired powders show probable impurity (111) peak of  $\text{CeO}_2$  (marked as x).



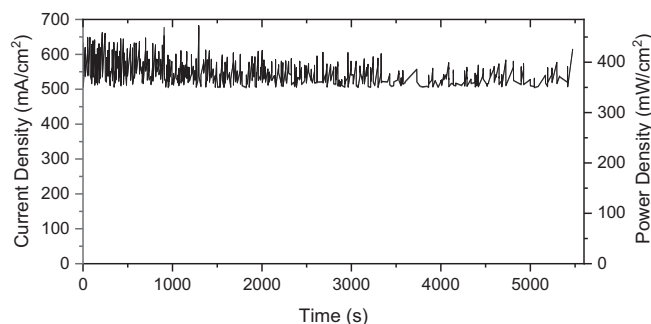
**Figure 3.** Electrochemical performance of the cell air /  $\text{H}_2 + 3 \text{ vol. } \% \text{ H}_2\text{O}$  as a function of temperature.



**Figure 4.** (a) Nyquist plots (not normalized) of cell at different operating temperatures (b) zoomed near origin (c) effect of oxidant flow on impedance spectrum at  $T = 600^{\circ}\text{C}$ .

fitting of impedance curves, the activation energy can be calculated from the slope of  $\ln(T/\text{resistivity})$  versus  $1000/T$  plots, as can be seen in Figure 5 for both the polarization and ohmic parts. This figure also shows total resistance at each temperature point. The approximately linear slope indicates that conduction mechanism remains same in the temperature range of  $600\text{--}850^{\circ}\text{C}$ .<sup>41</sup> If we consider the electrolyte contribution to be entirely from the ohmic part, then the activation energy is estimated to be around  $0.53\text{ eV}$  similar to the value reported previously.<sup>42</sup> Since 30% of the cathode is PCE, the activation energy of  $0.39\text{ eV}$  seems logical knowing that the value for pure LSCF is  $0.21\text{ eV}$ .<sup>38</sup>

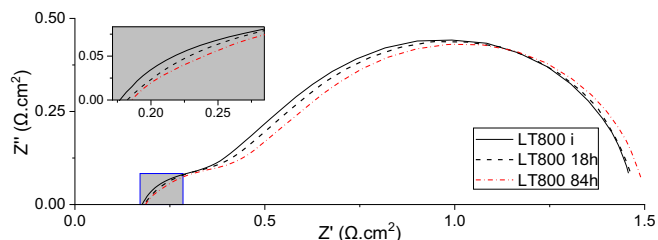
**Long-term degradation.**—Figure 6 shows the long-term run of the cell under the load for four consecutive days. The voltage is kept constant at  $0.7\text{ V}$  and the current is measured over time. Fluctuations in current are mainly due to imperfect current collector attachment especially at the anode side and coarsening of the electrode particles.<sup>43</sup> After four days, some slight variation was observed but there was no significant decrease in the performance compared to the start of the test.



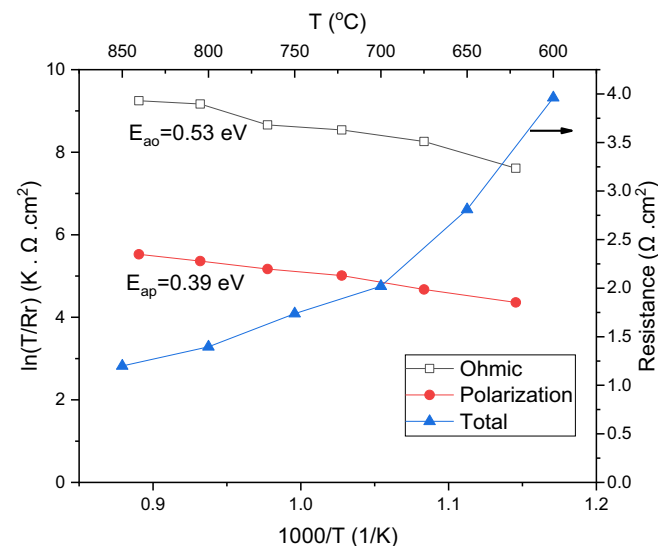
**Figure 6.** Long-term performance of cell under load of  $0.7\text{ V}$ .

Figure 7 shows the impedance spectrum initially, after 18 hours, and at the end of the test after four days, verifying no major degradation during the test. The ohmic contribution shows a slight increase in magnitude mainly due to imperfect attachment of mesh on the anode side. The activation portion of the polarization sees a hike which is mainly due to coarsening and lowering of the number of active sites. Polarization resistance is the main mechanism for degradation of the cell in agreement with other reported results.<sup>44–46</sup>

**Cell microstructure after electrochemical tests.**—Figure 8 shows the cross-section micrograph of a broken cell. The total thickness of the cell is estimated to be around  $410\text{ microns}$  with the AFL and electrolyte about  $8\text{ and }10\text{ microns}$ , respectively. The cathode is estimated to be  $25\text{ microns}$  in thickness. The far right side of Figure 8a shows the gold current collector. To achieve superior performance, it has been suggested to design a dual layer microstructure comprising an outer layer having coarser particles that act as a conduction layer while the second one near the electrolyte consists of fine particles known as the AFL that has a high electrocatalytic activity which results in a decrease in activation polarization.<sup>47</sup> Based on Figures 8a and 8b, the support is evenly distributed, although the high sintering temperature results in lower overall porosity and causes higher concentration polarization



**Figure 7.** Long-term run impedance spectrum.



**Figure 5.** Arrhenius plots of resistivity as a function of temperature and activation energy values calculated from ohmic and polarization part of impedance. The lines passing through symbols are only guide for the eyes. Where,  $E_{ao}$  = Activation energy due to ohmic contribution, and  $E_{ap}$  = Activation energy due to polarization contribution.

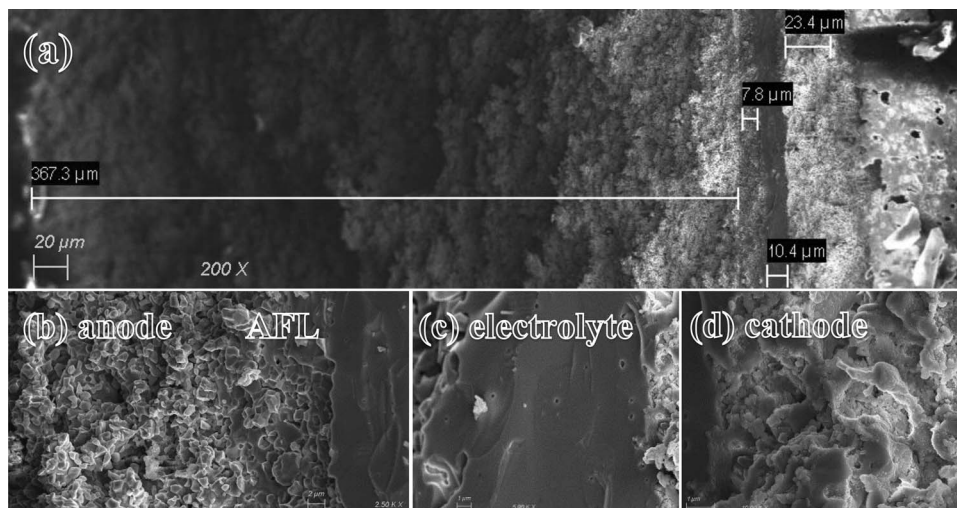


**Figure 8.** SEM images of cross-section view of the (a) whole cell, (b) from left to right, anode, AFL, electrolyte, (c) electrolyte, and (d) cathode after electrochemical testing in the air/H<sub>2</sub> + 3 vol.% H<sub>2</sub>O.

as previously observed. More tailoring of the microstructure seems essential, allowing the fuel to reach the functional layer more easily. The density of the AFL seems satisfactory, having enough active sites to convert hydrogen atoms to ion species. The electrolyte in Figure 8c shows fully dense electrolyte, which was achieved due to nano-grain precursors that were made using the sol-gel method. Adherence looks satisfactory with no gaps in between and a smooth transition from the support to the AFL and to the electrolyte. The composite cathode in Figure 8d consists of a BSCZGY matrix with LSCF particles dispersed in it. BSCZGY guarantees good bonding and ionic pathways for reactants and LSCF contributes electronic conductivity and is an excellent catalyst for the oxygen reduction reaction at the cathode generating a volumetric active region rather than a thin film one.

### Conclusions

A tubular SOFC based on a BSCZGY electrolyte was prepared using slip casting and dip coating. Investigations on chemical compatibility of the anode-electrolyte and electrolyte-cathode combinations revealed no major obstructive secondary phases due to the sintering process. The dependence of performance on temperature was studied, achieving maximum power density of 1 W/cm<sup>2</sup> at 850°C, one of the highest powers reported so far on tubular proton conductor SOFCs. The conductivity of the electrolyte changes only slightly above 800°C. Impedance analysis revealed the major part of the resistance comes from polarization, dominated by bulk diffusion, which is the bottleneck of performance and makes it essential to optimize cell microstructure. The micrograph also confirms this understanding. Satisfactory long-term results seen for four day run under load and impedance confirms negligible degradation. Detailed investigation of activation energies calculated both for the electrodes and electrolyte shows similar activation energies as reported in the literature. Therefore, this SOFC based on BSCZGY would be a suitable candidate for practical applications, especially in power generation and solid membrane reactors.

### Acknowledgment

Special thanks to the Natural Sciences and Engineering Research Council of Canada (NSERC) and InnoTech Alberta for funding this project. This research was supported from the Canada First Research Excellence Fund (CFREF) (to V. T. & K. S.) at the University of Calgary. V. T. also thanks the NSERC and Alberta Innovates for the support.

### ORCID

Taghi Amiri <https://orcid.org/0000-0001-6986-8164>  
 Jing-Li Luo <https://orcid.org/0000-0002-2465-7280>  
 Venkataraman Thangadurai   
<https://orcid.org/0000-0001-6256-6307>

### References

1. A. B. Stambouli and E. Traversa, *Renew Sust. Energ. Rev.*, **6**, 433 (2002).
2. M. Mamak, G. S. Métraux, S. Petrov, N. Coombs, G. A. Ozin, and M. Green, *J. Am. Chem. Soc.*, **125**, 5161 (2003).
3. R. M. Ormerod, *Chem. Soc. Rev.*, **32**, 17 (2003).
4. F. Tietz, H. P. Buchkremer, and D. Stöver, *Solid State Ionics*, **152–153**, 373 (2002).
5. S. Hossain, A. M. Abdalla, S. N. B. Jamain, J. H. Zaini, and A. K. Azad, *Renew Sust. Energ. Rev.*, **79**, 750 (2017).
6. R. Hempelmann, *Physica B: Condensed Matter*, **226**, 72 (1996).
7. J. W. Fergus, *J. Power Sources*, **162**, 30 (2006).
8. E. Fabbri, D. Pergolesi, and E. Traversa, *Chem. Soc. Rev.*, **39**, 4355 (2010).
9. Y. Guo, Y. Lin, R. Ran, and Z. Shao, *J. Power Sources*, **193**, 400 (2009).
10. H. Iwahara, *Solid State Ionics*, **28**, 573 (1988).
11. H. Iwahara, H. Uchida, K. Ono, and K. Ogaki, *J. Electrochem. Soc.*, **135**, 529 (1988).
12. H. Iwahara, T. Esaka, H. Uchida, and N. Maeda, *Solid State Ionics*, **3**, 359 (1981).
13. K. H. Ryu and S. M. Haile, *Solid State Ionics*, **125**, 355 (1999).
14. A. R. Hanifi, N. K. Sandhu, T. H. Etsell, J.-L. Luo, and P. Sarkar, *J. Power Sources*, **341**, 264 (2017).
15. K. Kreuer, *Solid State Ionics*, **97**, 1 (1997).
16. P. Babilo, T. Uda, and S. M. Haile, *J. Mater. Res.*, **22**, 1322 (2007).
17. T. Norby, *Solid State Ionics*, **125**, 1 (1999).
18. S. Haile, G. Stanoff, and K. Ryu, *Journal of Materials Science*, **36**, 1149 (2001).
19. S. Wienströer and H.-D. Wiemhöfer, *Solid State Ionics*, **101**, 1113 (1997).
20. S. C. Singhal, *Solid State Ionics*, **152–153**, 405 (2002).
21. A. L. Vincent, A. R. Hanifi, M. Zazulak, J.-L. Luo, K. T. Chuang, A. R. Sanger, T. Etsell, and P. Sarkar, *J. Power Sources*, **240**, 411 (2013).
22. Y. Bai, C. Wang, C. Jin, and J. Liu, *Fuel Cells*, **11**, 465 (2011).
23. S. C. Singhal, *Wiley Interdisciplinary Reviews: Energy and Environment*, **3**, 179 (2014).
24. X. Zhang, B. Lin, Y. Ling, Y. Dong, G. Meng, and X. Liu, *Int. J. Hydrogen Energy*, **35**, 8654 (2010).
25. N.-Q. Duan, D. Yan, B. Chi, J. Pu, and L. Jian, *Scientific reports*, **5**, 8174 (2015).
26. R. Kannan, K. Singh, S. Gill, T. Fürstenthaupt, and V. Thangadurai, *Scientific Reports*, **3**, 2138 (2013).
27. K. Singh, A. K. Baral, and V. Thangadurai, *Journal of Materials Science Research*, **5**, 34 (2016).
28. K.-Y. Park, T.-H. Lee, S. Jo, J. Yang, S.-J. Song, H.-T. Lim, J. H. Kim, and J.-Y. Park, *J. Power Sources*, **336**, 437 (2016).
29. A. R. Hanifi, N. K. Sandhu, T. H. Etsell, and P. Sarkar, *J. Am. Ceram. Soc.*, (2017).
30. K. Bae, H.-S. Noh, D. Y. Jang, J. Hong, H. Kim, K. J. Yoon, J.-H. Lee, B.-K. Kim, J. H. Shim, and J.-W. Son, *Journal of Materials Chemistry A*, **4**, 6395 (2016).
31. K. Singh, R. Kannan, and V. Thangadurai, *Int. J. Hydrogen Energy*, **41**, 13227 (2016).

32. M. Izuki, M. E. Brito, K. Yamaji, H. Kishimoto, D.-H. Cho, T. Shimonosono, T. Horita, and H. Yokokawa, *J. Power Sources*, **196**, 7232 (2011).
33. L. Kindermann, D. Das, H. Nickel, and K. Hilpert, *Solid State Ionics*, **89**, 215 (1996).
34. P. I. Dahl, H. L. Lein, Y. Yu, J. Tolchard, T. Grande, M.-A. Einarsrud, C. Kjølsteth, T. Norby, and R. Haugsrud, *Solid State Ionics*, **182**, 32 (2011).
35. H. G. Bohn and T. Schober, *J. Am. Ceram. Soc.*, **83**, 768 (2000).
36. Z. Shao and S. M. Haile, *Nature*, **431**, 170 (2004).
37. A. Braun and Q. Chen, *Nature Communications*, **8**, 15830 (2017).
38. L. da Conceição, A. M. Silva, N. F. P. Ribeiro, and M. M. V. M. Souza, *Mater. Res. Bull.*, **46**, 308 (2011).
39. J. Kilner, *Solid State Ionics*, **129**, 13 (2000).
40. N. Q. Minh, *J. Am. Ceram. Soc.*, **76**, 563 (1993).
41. J. Zhang, Z. Wen, S. Huang, J. Wu, J. Han, and X. Xu, *Ceram. Int.*, **34**, 1273 (2008).
42. W. Münch, K. D. Kreuer, G. Seifertli, and J. Majer, *Solid State Ionics*, **125**, 39 (1999).
43. M. A. Laguna-Bercero, A. R. Hanifi, H. Monzón, J. Cunningham, T. H. Etsell, and P. Sarkar, *Journal of Materials Chemistry A*, **2**, 9764 (2014).
44. A. Mai, M. Becker, W. Assenmacher, F. Tietz, D. Hathiramani, E. Ivers-Tiffée, D. Stöver, and W. Mader, *Solid State Ionics*, **177**, 1965 (2006).
45. H. Yokokawa, H. Tu, B. Iwanschitz, and A. Mai, *J. Power Sources*, **182**, 400 (2008).
46. E. D. Wachsman and K. T. Lee, *Science*, **334**, 935 (2011).
47. M. S. Khan, S.-B. Lee, R.-H. Song, J.-W. Lee, T.-H. Lim, and S.-J. Park, *Ceram. Int.*, **42**, 35 (2016).